PAPER

The role of doping in spin reorientation and terahertz spin waves in $SmDyFeO_3$ single crystals

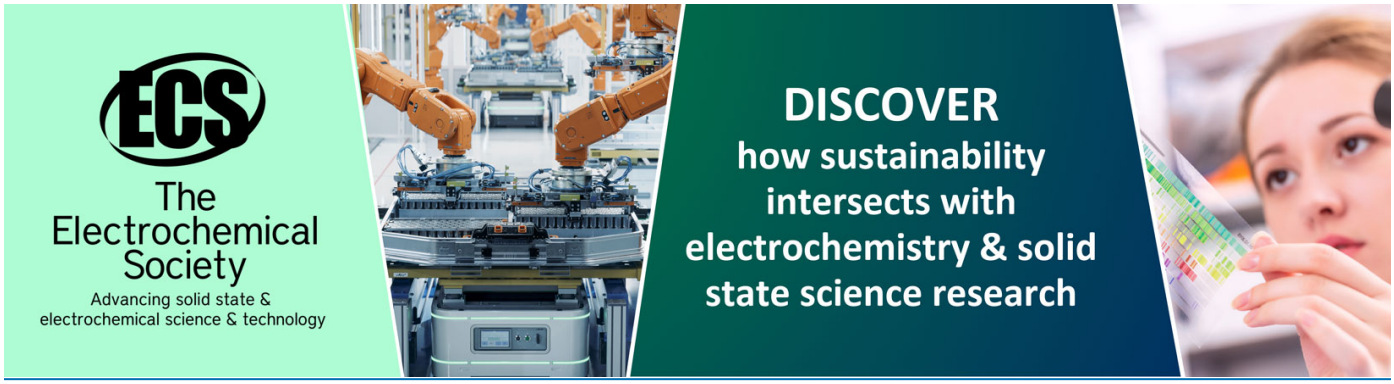

IOP Publishing Journal of Physics D: Applied Physics
J. Phys. D: Appl. Phys. **51** (2018) 024001 (9pp) https://doi.org/10.1088/1361-6463/aa9b5d

The role of doping in spin reorientation and terahertz spin waves in $SmDyFeO_3$ single crystals

Xiumei Liu[1], Zuanming Jin[1], Shunnong Zhang[1], Kailin Zhang[1], Weiyao Zhao[1], Kai Xu[1], Xian Lin[1], Zhenxiang Cheng[2], Shixun Cao[1] and Guohong Ma[1]

[1] Department of Physics, Shanghai University, 99 Shangda Road, Shanghai 200444, People's Republic of China
[2] Institute for Superconducting and Electronic Materials, University of Wollongong, Wollongong, New South Wales 2500, Australia

E-mail: physics_jzm@shu.edu.cn, sxcao@shu.edu.cn and ghma@staff.shu.edu.cn

Received 15 September 2017, revised 12 November 2017
Accepted for publication 17 November 2017
Published 12 December 2017

Abstract

In this work, by using terahertz time-domain spectroscopy (THz-TDS), we investigate the temperature range of the SRT, and the resonant frequency and relaxation time of the THz spin waves in $Sm_xDy_{1-x}FeO_3$ single crystal. We show that the resonant frequency of the FM mode (measured at 40 K) increases linearly with the Sm dopant concentration within the range from $x = 0.5$ to 0.7. The temperature- and dopant-induced changes of the magnetic anisotropy of Fe^{3+} ions are accessed by the resonant frequency shifts. Upon cooling, the lifetime of oscillations in the AFM mode increases exponentially and can be subtly tuned by varying the Sm dopant. These results lead to an improved understanding of dopant-tuned spin wave dynamics and magnetoanisotropy parameter in rare-earth orthoferrites.

Keywords: terahertz time-domain spectroscopy, rare-earth orthoferrites, spin reorientation transition, spin wave dynamics

(Some figures may appear in colour only in the online journal)

1. Introduction

Rare earth orthoferrites ($RFeO_3$, R = rare earth) possessing two magnetic ions, rare earth R^{3+} and iron Fe^{3+} ions, crystallize in the orthorhombic distorted perovskite structure with the Pbnm space group [1]. As a functional material family, $RFeO_3$ has attracted increasing attention in recent years due to its novel properties and capabilities, including ultrafast optomagnetic recording [2–5], laser-induced thermal spin reorientation [3, 6], spin mode resonant excitation, coherent control of magnetization dynamics by the magnetic field of terahertz pulses [7–13], and magnetism-induced ferroelectric multiferroic behavior [14–18]. The two metallic ions provide three magnetic interactions, including Fe^{3+}–Fe^{3+}, R^{3+}–R^{3+}, and Fe^{3+}–R^{3+} couplings. This series of compounds has been found to possess G-type antiferromagnetic ordering based on the Fe^{3+}–Fe^{3+} interaction, and the resonant frequency of the magnetic moments extends into the terahertz regime due to the strong internal magnetic field [19, 20]. In addition, the Fe^{3+} spin directions are slightly canted with respect to one another, owing to the antisymmetric Dzyaloshinsky–Moriya (DM) interaction [21, 22]. It should be noted that the R–R interaction will only be activated at 10 K or less, which contributes to the long-range magnetic ordering of the rare earth ions.

Due to symmetry considerations and the antiferromagnetic nature of the coupling between the ions, there are three magnetic configurations allowed for the Fe^{3+} sublattices: the Γ_1, Γ_2, and Γ_4 configurations with different antiferromagnetic directions. In the Γ_1 configuration, there is no net magnetization **M** along any direction, and the major **G**-type antiferromagnetic vector points along the b-axis. The Γ_2 configuration is

characterized by pointing of the net moment **M** along the *a*-axis and the major **G**-type antiferromagnetism vector along the *c*-axis. Triggered by temperature, a spin reorientation transition (SRT) (i.e. a rotation of the macroscopic magnetization by 90 degrees) takes place from the low temperature (LT) phase (Γ_2) to the high temperature (HT) phase (Γ_4). In the Γ_4 configuration, the net moment **M** is aligned along the *c*-axis and the **G**-type antiferromagnetism vector along the *a*-axis. The origin of the SRT is found in the competition between different spin configurations, which possess different free energy [23]. The temperature-dependent magneto-crystalline anisotropy of the R^{3+}–Fe^{3+} (4f–3d electrons) interaction is the dominant mechanism for the thermally-induced SRT in RFeO$_3$. The SRT has been investigated in NdFeO$_3$, TmFeO$_3$, and SmFeO$_3$, where there is a magnetic configuration transition between Γ_2 and Γ_4 via the intermediate phase Γ_{24} [7, 24, 25]. Interestingly, in DyFeO$_3$, the magnetic configuration switches from Γ_1 to Γ_4 as the temperature increases [26].

Recently, Baierl *et al* showed that phase-locked THz pulses, which can abruptly change the orbital state of electrons, can lead to a sudden modification of the magnetic anisotropy and then trigger magnon oscillations with large amplitudes [27]. The strong coupling between the electronic orbital states and the ordered spin states exactly occurs within the temperature range of the SRT. In most RFeO$_3$ compounds, however, the spin reorientation transition temperatures are fixed and relatively low, making it inconvenient to trigger the magnons with the electric-field of the THz pulse. In addition, the dynamics of spin waves with respect to different types of R^{3+}–Fe^{3+} coupling remains unknown so far. To this end, based on the knowledge that SmFeO$_3$ has the SRT temperature of 450–480 K and DyFeO$_3$ has the SRT temperature of 38 K, we therefore selected the dysprosium-samarium orthoferrites ($Sm_xDy_{1-x}FeO_3$) as our sample system.

2. SRT observed with terahertz time domain spectroscopy (THz-TDS)

Terahertz time-domain spectroscopy (THz-TDS) has been proved to be an effective tool to excite and probe magnetic- and electronic-dipole transitions [28–30]. In many antiferromagnetic materials, intrinsic magnetic fields put the spin waves into the THz range. Impulsive excitation of spin precession by THz pulses is free from hot electron excitations due to the small photon energy [31, 32]. The most recent developments in the generation of intense THz pulses have made it possible to drive the elemental modes into the nonlinear regime [33, 34].

The spin precessions are non-thermally excited and manipulated by the sub-picosecond magnetic-field component of the THz wave. From the point of view of classical physics, when the THz pulse enters a magnetically ordered sample, a magnetic moment in the sample experiences a Zeeman torque, $\mathbf{T} = \gamma\mathbf{M} \times \mathbf{H}_{\mathrm{THz}}$, where γ and $\mathbf{H}_{\mathrm{THz}}$ are the gyromagnetic constant of the sample and the impulsive magnetic field of the incident THz pulse, respectively [35]. This torque tilts the magnetic moment out of equilibrium. After being tilted, the magnetic moment starts to precess around the internal effective magnetic field. The induced precession of the macroscopic magnetization is expected to radiate a free induction decay (FID) signal at the magnetic resonance frequency, the amplitude of which is proportional to the tipping angle of the spin and the excitation magnetic field strength. On the other hand, from the point of view of quantum physics, a simplified two-level quantum transition model can be used to describe the resonant absorption and radiation in antiferromagnets [36, 37]. The magnetic field of a broadband THz pulse with angular frequency ω couples with the ground state and excited state, and then excites the magnetic dipole transition. Typically, there are two spin modes in the (sub-) THz range, i.e. the quasi-ferromagnetic mode (FM) and the quasi-antiferromagnetic mode (AFM), which can be excited when the $\mathbf{H}_{\mathrm{THz}}$ is perpendicular and parallel to the macroscopic magnetization of the crystal, respectively [38, 39]. The FM mode resonance can be interpreted as a precession of the macroscopic magnetization, AFM mode, on the other hand, can be seen as a fluctuation in magnitude of the magnetization.

The mechanism for the observation of the SRT is indeed based on the rotation angle between **M** and $\mathbf{H}_{\mathrm{THz}}$. As shown in figure 1(a), in the case of the *b*-cut sample that we used, the terahertz pulse propagates along the *b*-axis with the $\mathbf{H}_{\mathrm{THz}}$ parallel to the *c*-axis, and then the transmitted THz wave is detected. With temperature is decreasing, the macroscopic magnetization **M** rotates to **M**′ within the *a*-*c* plane. The AFM mode is excited with the magnetic component of the THz pulse parallel to **M**, and the detected amplitude transmission of the AFM mode is proportional to $\mathbf{M}(T)(\cos\theta)$ [2], where $\theta = 0°$ and $\theta = 90°$ correspond to the *c*- and *a*-axis directions, respectively. In contrast, the detected amplitude transmission of the FM mode is proportional to $\mathbf{M}(T)(\sin\theta)$ [2]. In this way, by monitoring the temperature dependence of the amplitude and frequency of the THz FID signal, the full dynamical information on the magnetic vector of RFeO$_3$ can be determined by THz-TDS [40, 41].

In this paper, using a single THz pulse, we directly create a spin wave on an ultrafast timescale. The SRT temperatures can be determined by recording the amplitude of the THz FID signal as a function of temperature, which increases linearly in Sm-rich samples ($x > 0.2$). We demonstrate that the FM spin resonances are significantly softened upon approaching the temperature range of SRT. The resonant frequency of the FM mode (measured at 40 K) increases linearly with the Sm-dopant concentration, while, the frequency of the THz spin waves with the AFM resonance is almost independent of temperature and dopant. We note that a decrease in the AFM spin resonant frequency is only observed in a Dy-rich sample. Furthermore, the relaxation time of the AFM spin waves increases during cooling, with different rates of increase. This observation is strongly determined by the Dy^{3+} dopant concentration. In our approach, we add R^{3+} dopant as a novel degree of freedom for manipulation of the complicated 4f–3d electron interactions between R^{3+}–Fe^{3+} ions, leading to dopant-tuned amplitude, frequency, and lifetime of the resulting THz spin waves. Our results are noteworthy owing to the fundamental physics and potential applications of spintronics.

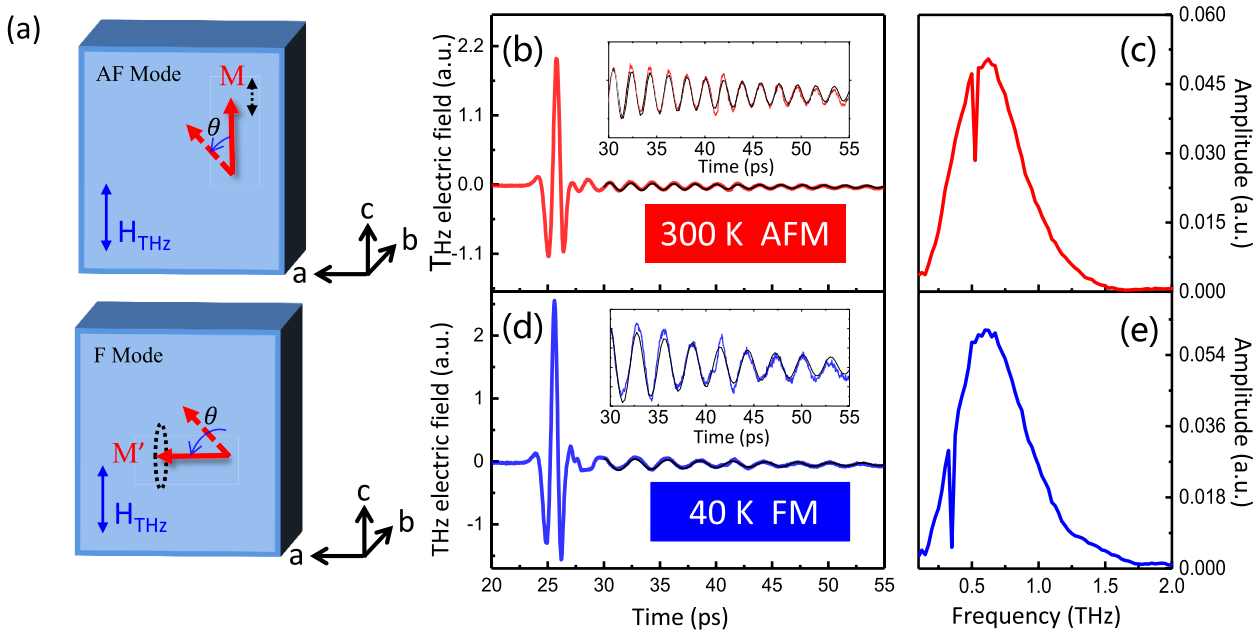

Figure 1. (a) Mechanism of SRT measurement by THz-TDS. The magnetic-field of the incident THz pulse is set to be along the *c*-axis of the crystal. The AFM magnetization vector is not plotted in the schematic illustration. The THz waveform is transmitted through a *b*-cut $Sm_{0.5}Dy_{0.5}FeO_3$ crystal at (b) 300 K and (d) 40 K. The main part of the broadband THz pulse is centered at 26 ps, and it features a temperature independent refractive index without phase shifting. The insets are magnifications of the amplitude tail of the THz pulse. (c), (e) The Fourier transform of the THz electric field in the time range from 20 to 55 ps at 300 K and 40 K, respectively.

3. Samples and experiments

Our single crystals of $Sm_xDy_{1-x}FeO_3$ (SDFO) with $x = 0.3$–0.7 were grown by an optical-floating-zone method (Crystal System Inc., type FZ-T-10000-H-VI-P-SH). The compounds for the feed and seed rods were prepared by the solid state reaction of the raw materials Sm_2O_3 (99.9%), Dy_2O_3 (99.9%), and Fe_2O_3 (99.99%), with the proper cation stoichiometry calculated for the target compound. The temperature of the molten zone was controlled by adjusting the power of the lamps. During the growth process, the molten zone moved upwards at a rate of 1–3.5 mm h^{-1}, with the seed rod (lower shaft) and the feed rod (upper shaft) counter-rotating at 30 rpm in flowing air [23, 42]. More detailed x-ray diffraction information can be found in [23]. The SDFO single crystals were polished on both sides with thickness of 1.10 mm.

Our THz-TDS measurements in the standard transmission configuration were conducted on the *b*-cut SDFO crystals in the frequency range of 0.1–2 THz over the temperature range from 40–300 K. Briefly, the output of a mode-locked Ti: sapphire laser, with pulse duration of 100 fs, centered wavelength of 800 nm, and repetition rate of 80 MHz (Mai Tai HP-1020, Spectra-Physics), was used to generate and detect the THz transient. The emitter and detector of the THz wave were dipole type low-temperature-grown GaAs photoconductive antennas. The polarization of the THz radiation was vertical, which was perpendicular to the photoconductive antennas. No external static magnetic field was applied on the sample during the measurement. The sample was installed in a cold finger cryostat with two THz-transparent windows, for which the temperature was tunable in the range of 40–300 K with best resolution of 1 K.

4. Results and discussion

Figures 1(b) and (d) present the typical THz waveforms transmitted through a representative sample of a *b*-cut $Sm_{0.5}Dy_{0.5}FeO_3$ single crystal, in the high temperature phase (300 K) and the low-temperature phase (40 K), respectively. When the crystal is below the Néel temperature and above the reorientation temperature, the magnetic system is located in the Γ_4 phase [23]. Following the main transmitted THz pulses, precession of the magnetization is observed due to the FID signal present in the long-tailed oscillation component, in the high temperature phase (the red line in figure 1(b)). In this case, as the magnetic-field of the incident THz pulse is parallel to the net magnetic moment **M** of $Sm_{0.5}Dy_{0.5}FeO_3$ at room temperature, the slowly decaying oscillation is caused by the FID signal, leading to the AFM spin resonance mode at a frequency of 0.52 THz, which can be clearly seen as an absorption dip in the corresponding Fourier spectrum in figure 1(c). At the temperature of 40 K, the oscillation period is changed from 1.92 ps to 2.86 ps, which is observed as a narrow resonance dip at the frequency of 0.35 THz (figure 1(e)). This can be explained by the rotation of the macroscopic magnetization **M** from the *c*-axis towards the *a*-axis, as described earlier, i.e. the $Sm_{0.5}Dy_{0.5}FeO_3$ is transformed into Γ_2 magnetic phase. In this case, the incident THz pulse was expected to excite the FM mode, as shown in figure 1(a).

Let us now discuss the THz spin wave excitation in the family of single crystals $Sm_xDy_{1-x}FeO_3$ (SDFO) with $x = 0.3$, 0.5, 0.6, and 0.7. Figure 2 shows the amplitude mapping of FID signals in the long-tailed oscillation component of the THz spin wave as a function of temperature. All the samples studied here are *b*-cut, with $\mathbf{H}_{THz}//c$. Therefore, the

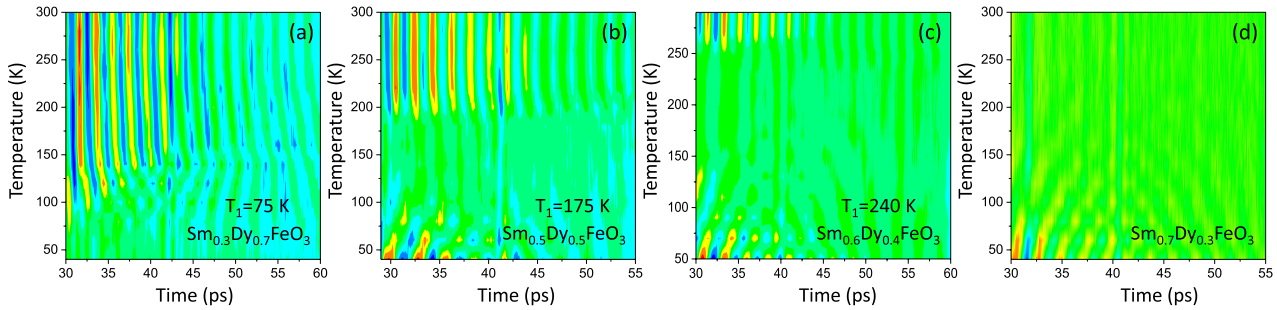

Figure 2. Amplitude mapping of the oscillating part of the FID signal, as a function of the temperature (40–300 K), for (a) $Sm_{0.3}Dy_{0.7}FeO_3$, (b) $Sm_{0.5}Dy_{0.5}FeO_3$, (c) $Sm_{0.6}Dy_{0.4}FeO_3$, and (d) $Sm_{0.7}Dy_{0.3}FeO_3$, respectively, in the time window of 30–55 ps.

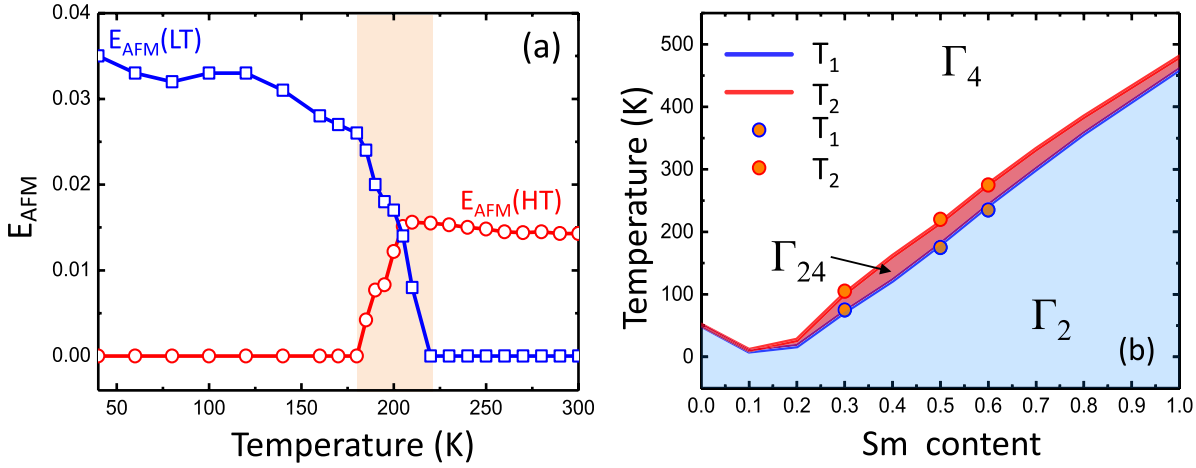

Figure 3. (a) Temperature dependence of the amplitude of AFM-mode emission with the THz magnetic field along the *a*-axis (open blue squares) and the *c*-axis (open red circles) of the *b*-cut $Sm_{0.5}Dy_{0.5}FeO_3$ crystal. The shaded area shows the SRT temperature interval, within the magnetic mesophase Γ_{24}. (b) SRT temperatures for the SDFO single crystal family versus Sm concentration. Points are extracted from the THz experimental results, while the solid lines come from the temperature dependence of magnetization measurement.

AFM mode should be resonantly excited in the magnetic configuration of Γ_4 phase. As shown by the bird's eye view plots in figure 2(b), in the case of Sm concentration $x = 0.5$ ($Sm_{0.5}Dy_{0.5}FeO_3$), it is clearly seen that the FID signal with AFM mode is in the high temperature phase (Γ_4). The amplitude of the FID radiation decreases with decreasing temperature and disappears around 175 K. When the sample goes through the reorientation transition into the low temperature phase (Γ_2), the vector **M** is reoriented along the *a*-axis, and then the FM mode will be excited. Herein, we find that the FM mode appears when the temperature decreases further below 100 K. The absorption and frequency of the AFM mode as a function of temperature will be discussed later. If we reduce the Sm concentration down to $x = 0.3$ ($Sm_{0.3}Dy_{0.7}FeO_3$), the disappearance temperature of the AFM mode shifts down to around 75 K. It is notable that, in the current temperature range, we cannot observe the FM mode in the low temperature phase, while, in the case of $Sm_{0.6}Dy_{0.4}FeO_3$, the AFM oscillation is present in the high temperature phase, which disappears around 250 K, corresponding to the end of the spin reorientation transition, and the FM mode can be observed below 100 K. Furthermore, in the case of $Sm_{0.7}Dy_{0.3}FeO_3$, as shown in figure 2(d), we can only see the FM mode below 100 K, because the temperature of the AFM mode is beyond the temperature range used in our current work.

To obtain a deeper insight into the SRT dynamics, we show typical data for a THz wave transmitted through the *b*-cut $Sm_{0.5}Dy_{0.5}FeO_3$ single crystal. We systematically study the amplitude of the AFM mode emission ($\mathbf{E}_{AFM}$) as a function of temperature for both $\mathbf{H}_{THz}//c$ (red circles) and $\mathbf{H}_{THz}//a$ (blue squares) excitation configurations, respectively, as shown in figure 3(a). In the case of $\mathbf{H}_{THz}//c$, when the temperature is higher than 220 K, it is seen that the magnitude of $\mathbf{E}_{AFM}$(HT) reaches its maximum and is almost temperature-independent, indicating that the Γ_4 magnetic phase is very stable. When the temperature is lower than 220 K, the $\mathbf{E}_{AFM}$ decreases with temperature is decreasing. Then, the magnetic configuration is located in the metastable state of Γ_{24} phase. When the temperature is reduced further below 175 K, $\mathbf{E}_{AFM}$ disappears completely as the **M** vector points along the *a*-axis, which means that the magnetic phase has already been transformed into Γ_2 phase. With the excitation geometry of $\mathbf{H}_{THz}//a$ (blue squares), the AFM mode is activated below 220 K and increases slightly further below 175 K, up to $\mathbf{E}_{AFM}$(LT). As a result, two critical temperatures can be obtained, $T_2 = 220$ K and $T_1 = 175$ K, corresponding to the SRT temperatures from Γ_4 to Γ_{24} and from Γ_{24} to Γ_2, respectively. T_1 is the temperature where the SRT begins from the low-temperature configuration, and T_2 is the final temperature of the SRT. We note that, when measured by THz, $\mathbf{E}_{AFM}(LT) > \mathbf{E}_{AFM}(HT)$, which is in good agreement

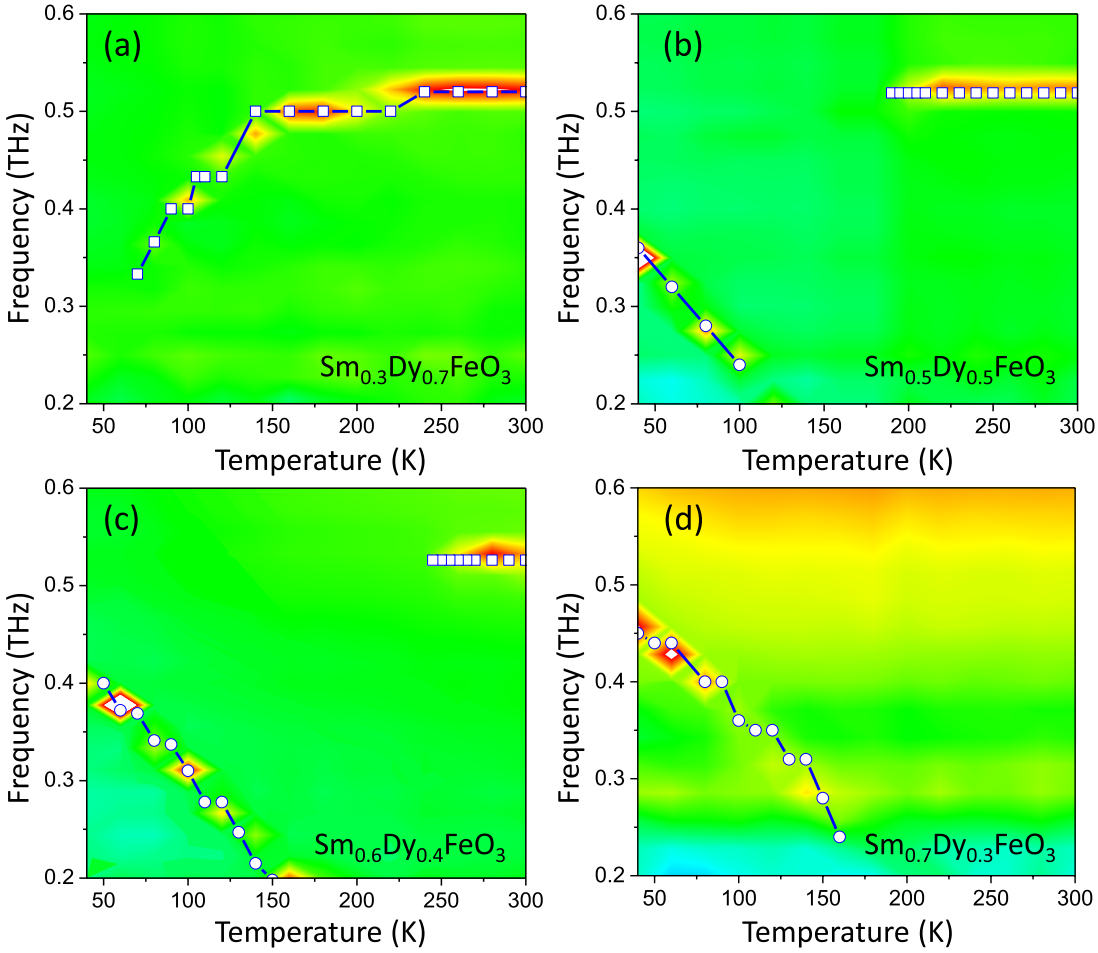

Figure 4. The amplitude mapping of resonant frequencies (AFM mode (squares) and FM mode (circles)) of the *b*-cut $Sm_xDy_{1-x}FeO_3$ crystal as a function of temperature, for (a) $Sm_{0.3}Dy_{0.7}FeO_3$, (b) $Sm_{0.5}Dy_{0.5}FeO_3$, (c) $Sm_{0.6}Dy_{0.4}FeO_3$, (d) $Sm_{0.7}Dy_{0.3}FeO_3$.

with the zero-field-cooling (ZFC) magnetization measurement, yielding the magnetization values $\mathbf{M}_a$ (50 K) and $\mathbf{M}_c$ (300 K), which are around 2.7 and 1.1 emu g^{-1}, respectively [23]. The THz measured SRT temperatures are summarized in figure 3(b), and we find that the SRT temperature increases linearly in Sm-rich samples ($x > 0.2$), which is in excellent agreement with the ZFC measurements. It is well known that $SmFeO_3$ has a high SRT temperature (~480 K), owing to the strong Sm^{3+}–Fe^{3+} interaction compared with the anisotropic part of the Fe^{3+}–Fe^{3+} interaction. The dopant of Dy into Sm sites of $SmFeO_3$ will naturally reduce the intensity of the Sm^{3+}–Fe^{3+} interaction and thus decrease the SRT temperature in the SDFO single crystal.

We used the terahertz transient not only to determine the SRT region, but also to investigate the resonant frequencies of the FM and AFM modes as a function of temperature and dopant concentration. Figure 4 shows the temperature dependence of the resonant frequencies for the FM and the AFM modes for $Sm_{0.3}Dy_{0.7}FeO_3$, $Sm_{0.5}Dy_{0.5}FeO_3$, $Sm_{0.6}Dy_{0.4}FeO_3$, and $Sm_{0.7}Dy_{0.3}FeO_3$. For the Sm-rich ($x \geqslant 0.5$) samples, the resonant frequency of the AFM mode remains almost constant with decreasing temperature, while the softening of the FM mode can be clearly seen as the temperature approaches the spin reorientation range.

In the two-sublattice model, two spin modes with different resonant frequencies are [43]

$$(\hbar\omega_{\mathrm{FM}})^2 = 24JS\left[2\left(K_x - K_z\right)S\right] \tag{1}$$

$$(\hbar\omega_{\mathrm{AFM}})^2 = 24JS\left[6DS\ \tan\beta + 2K_xS\right] \tag{2}$$

where β is the antiferromagnetic angle between the Fe^{3+} magnetic moment of each spin sublattice and the crystal axis, and has a magnitude of several mrads. K_x and K_z are the second-order anisotropic constant along a and c crystal axes, respectively. J and D are the isotropic Heisenberg and antisymmetric DM interaction constants, respectively. S is the spin moment of the Fe^{3+} sublattice.

As equation (1) shown, the resonant frequency of FM mode (the rocking motion of antiparallel spin moments in the xz plane) depends on the difference in the anisotropic constant ($K_x - K_z$). Equation (2) shows that the energy of AFM mode (the twisting motion about the antiferromagnetic axis) is sensitive to (i) anisotropic constant K_x and (ii) the spin canting ($D\tan\beta$). Near the SRT temperature region, the term ($K_x - K_z$) is approaching zero, which leads to the softening of the FM mode [8, 44], as shown in figures 4(b)–(d). In the case of the AFM mode, however, $\hbar\omega_{\mathrm{AFM}}$ is proportional to the K_x. The resonance frequency of the AFM mode is almost

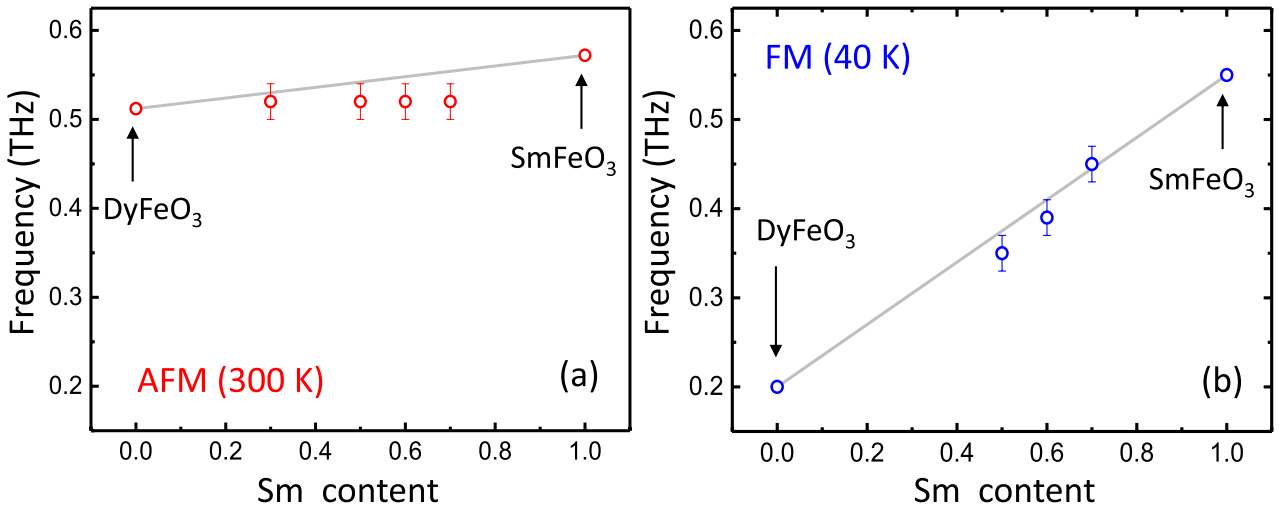

Figure 5. The resonant frequency of the *b*-cut $Sm_xDy_{1-x}FeO_3$ single crystals as a function of Sm concentration. In two cases: (a) AFM mode is probed at the temperature of 300 K and (b) FM mode is probed at the temperature of 40 K.

temperature independent, which indicates that K_x is hard to change by decreasing the temperature. It is interesting to note that for the Dy-rich sample ($Sm_{0.3}Dy_{0.7}FeO_3$), the resonant frequency of the AFM mode shows a remarkably inflection in the low temperature range ($T < 150$ K), as shown in figure 4(a). Our results indicate that when the Dy concentration is predominant, the anisotropy part of the Fe^{3+}–Fe^{3+} interaction for K_x is effectively reduced. Meanwhile, in the Dy-rich SDFO single crystal, the R^{3+}–Fe^{3+} interaction energy is significantly reduced, as mentioned in connection with the temperature of the SRT earlier.

Let us now further consider the Sm concentration dependence of the resonant frequencies of the AFM and FM modes in the SDFO single crystal. As presented in figure 5(a), the resonant frequency of the AFM mode at room temperature (300 K) is 0.52 ± 0.02 THz, which shows the dopant independence within the range of $x = 0.3$–0.7. The resonant frequency of 0.52 THz is located exactly within the range of the resonant frequencies measured for $DyFeO_3$ (0.512 THz) and $SmFeO_3$ (0.572 THz), as shown in the same figure. In contrast, it is important to stress that the resonant frequency of the FM mode of SDFO single crystal at 40 K undergoes a linear increase from 0.35 THz to 0.45 THz over the range of Sm concentrations $x = 0.5$–0.7. It should be mentioned that these three resonant frequencies are located exactly on the line between 0.20 THz and 0.55 THz, which correspond to the values of the FM modes for $DyFeO_3$ and $SmFeO_3$, respectively, as shown in figure 5(b). A simplified two-level quantum transition model can be used to describe the resonant absorption and radiation in $RFeO_3$. The strong exchange field induces fine structure, yielding the ground state and excited state [37]. Our findings indicate the correlation between the band energy difference ($\hbar\omega$) and the Sm^{3+} composition (x) of SDFO single crystals, which is expressed as a monotonic continuous function, $\hbar\omega_{\mathrm{FM}}^{\mathrm{Sm_xDy_{1-x}FeO_3}} = x\hbar\omega_{\mathrm{FM}}^{\mathrm{SmFeO_3}} + (1-x)\,\hbar\omega_{\mathrm{FM}}^{\mathrm{DyFeO_3}}$. Thus, we can directly estimate the variation of the FM resonant frequency with the Sm^{3+} composition.

Proceeding with the analysis, in the high temperature phase (Γ_4), calculated according to equation (2), $(\hbar\omega_{\mathrm{AFM}})^2 \propto [D\tan\beta + K_x]$. For the case of Γ_2, however, $(\hbar\omega_{\mathrm{FM}})^2 \propto [K_x - K_z]$. We observe that the frequency of the FM mode is much more sensitive to the Sm concentration, which indicates that (1) the magnitude of K_x is larger than that of K_z, and (2) the Sm-Dy concentration changes K_z more significantly than K_x. Figure 6(a) shows the calculated difference in the anisotropic constant $|K_x - K_z|$ as a function of Sm concentration, which is converted from the measured FM mode frequency shift (figure 5(b)) by using equation (1). The anisotropy change is normalized with the anisotropy of $SmFeO_3$. It can be seen that the decrease of Sm concentration (i.e. increase of Dy concentration) leads to a decrease of the anisotropy parameter $|K_x - K_z|$. In addition, one can notice that $|K_x - K_z|$ in $Sm_{0.5}Dy_{0.5}FeO_3$, $Sm_{0.6}Dy_{0.4}FeO_3$ and $Sm_{0.7}Dy_{0.3}FeO_3$ decrease almost linearly with increasing temperature, as shown in figure 6(b). The anisotropic constant of the Fe^{3+} spins in the orthoferrites are known to be dependent on the paramagnetic moment of the R ions. Therefore, we can give a tentative explanation that the redistribution of *4f* electrons in the mixed SDFO single crystal changes the anisotropy parameter $|K_x - K_z|$ and then leads to a frequency shift of the Fe^{3+} spin precessions. With the THz time-domain spectroscopy, the interaction energy of R^{3+}–Fe^{3+} not only can be accessed by the temperature range of the SRT, but also can be determined by the shift in the frequency of the spin-wave resonance in SDFO single crystal, depending on the temperature and/or dopant concentration.

We now make one step further in our analysis, and finally discuss the impact of Sm-Dy concentration on relaxation of spin waves. As mentioned above, the experimentally collected THz signals in figure 1 is the superimposition of the absorbed transmitted THz pulse and a sinusoidal FID signal. The THz FID signal radiated from the magnetic dipole is given by [36]

$$\mathbf{E}_{\mathrm{THz}} \propto A \times \sin(\omega t + \varphi_0)\mathrm{e}^{-t/\tau}, \qquad (3)$$

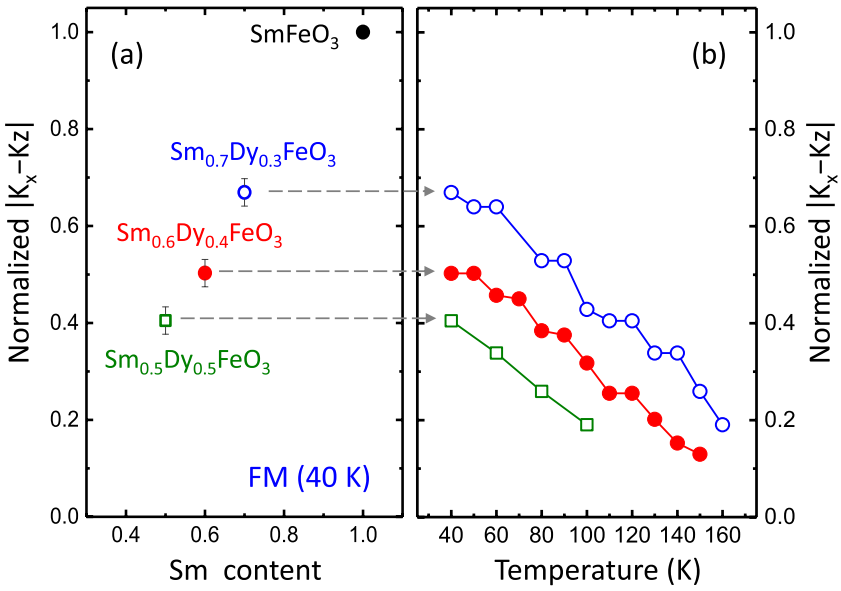

Figure 6. (a) The Sm content dependent anisotropy change $|K_x - K_z|$ in $Sm_xDy_{1-x}FeO_3$ at 40 K. The anisotropy change is normalized with the anisotropy of $SmFeO_3$. (b) Temperature dependence of the normalized anisotropy change $|K_x - K_z|$ in $Sm_{0.5}Dy_{0.5}FeO_3$, $Sm_{0.6}Dy_{0.4}FeO_3$, and $Sm_{0.7}Dy_{0.3}FeO_3$, which are converted from the frequency shifts shown in figure 4.

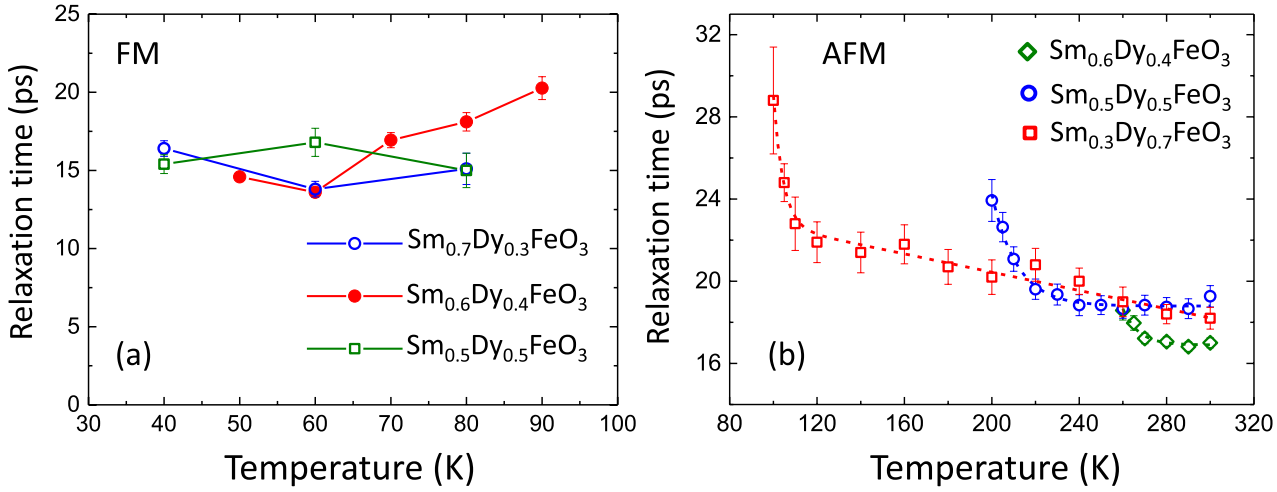

Figure 7. (a) Temperature-dependent relaxation time of the FM mode of $Sm_{0.5}Dy_{0.5}FeO_3$, $Sm_{0.6}Dy_{0.4}FeO_3$, and $Sm_{0.7}Dy_{0.3}FeO_3$. (b) The relaxation time of the AFM mode as a function of temperature varies with the Sm concentration: $x = 0.3$, 0.5, and 0.6. Dashed lines are the exponential fits.

where A, τ, ω, and φ_0 are the amplitude, relaxation time, resonant frequency, and initial phase of the THz spin waves (magnons). As shown by the solid lines in the insets of figures 1(b) and (d), the amplitude decay of the FM and AFM magnon oscillations in the time window of 30–55 ps can be fitted by equation (3) very well.

Figure 7 summarizes the extracted relaxation time τ of FM and AFM in SDFO as a function of temperature. Figure 7(a) shows the relaxation time of FM, τ for $Sm_{0.5}Dy_{0.5}FeO_3$, $Sm_{0.6}Dy_{0.4}FeO_3$, $Sm_{0.7}Dy_{0.3}FeO_3$ are very close within our investigated temperature region of 40–80 K, while, it can be clearly found that the relaxation time of AFM gradually increases as the temperature decreases. During the cooling process, as can be seen, the increasing trend for the relaxation time versus temperature of the AFM mode in SDFO single crystal strongly depends on the Sm concentration, $x = 0.3$, 0.5, and 0.6. As shown in figure 7(b), for the Sm-rich samples ($x = 0.5$, 0.6), we fit the temperature dependence of the relaxation time $\tau(T)$ to a phenomenology exponential function $\tau(T) \propto A_0 + A_1 * \exp\left(-\frac{T}{T_c}\right)$. The parameter T_c describes the increasing trend of $\tau(T)$, with $T_c = 11.6$ K and 7.1 K for $Sm_{0.5}Dy_{0.5}FeO_3$ and $Sm_{0.6}Dy_{0.4}FeO_3$, respectively. This indicates that the increasing trend of $\tau(T)$ for $Sm_{0.6}Dy_{0.4}FeO_3$ is slight faster than that for $Sm_{0.5}Dy_{0.5}FeO_3$. Note that for the Dy-rich sample $Sm_{0.3}Dy_{0.7}FeO_3$, we find that $\tau(T)$ increases gradually from 300 K to 150 K, and then a faster rise occurs below 150 K. Fitting this trend of $\tau(T)$ to a phenomenology double-exponential form $\tau(T) \propto A_1 * \exp\left(-\frac{T}{T_{c1}}\right) + A_2 * \exp\left(-\frac{T}{T_{c2}}\right)$ yields $T_{c1} = 4.5 \pm 0.5$ K and $T_{c2} = 960 \pm 50$ K. Our observations suggest that (1) the decay dynamics of SDFO single crystal

are strongly related to the temperature, which could be explained by the spin wave decaying by transferring its energy to the lattice system [45, 46]. (2) The much faster increasing trend for $\tau(T)$ below 150 K in the Dy-rich crystal could be assigned to the influence of the dominated Dy^{3+}–Fe^{3+} interaction, evidenced by the softening of AFM mode below 150 K (figure 4(a)). Hence, we conclude that the spin-lattice thermalization depends critically on the R^{3+}–Fe^{3+} interaction and temperature. Our experimental results guide the physical picture that the R^{3+}–Fe^{3+} interaction tuned magnon-phonon scattering plays a vital role in the relaxation dynamics of the spin waves. Certainly, we would like to mention that strong THz-pump mid-infrared Faraday rotation measurement [47, 48], and coherent 2D THz magnetic resonance spectroscopy [49] are required to get insights into the magnon-phonon scattering systematically.

5. Conclusion

To summarize, we have demonstrated dopant-controlled spin-reorientation effects in the SDFO single crystal family, by using terahertz time-domain spectroscopy. The SRT temperature region can be determined from the THz transient, which increases linearly with Sm-rich dopant. Most importantly, the resonant frequency of the FM mode (measured at 40 K) increases almost linearly with the Sm dopant concentration within the range from $x = 0.5$ to 0.7. In addition, the AFM mode frequency of the Dy-rich $Sm_{0.3}Dy_{0.7}FeO_3$ starts to soften when the temperature is below 150 K. Through the resonance frequency shifts of the FM mode, we estimate the changes in the anisotropic constant of the iron spins as function of temperature and concentration of Sm dopant. Finally, the relaxation time of the oscillations of the AFM spin mode increases exponentially upon cooling the SDFO single crystals, which is subtly tuned by varying the Sm dopant. Our findings give experimental insights into the THz spin wave dynamics, with complicated R^{3+}–Fe^{3+} interaction and magnon-phonon scattering, and may open up potential applications in future spin-based devices.

Acknowledgments

This work is supported by the National Natural Science Foundation of China (NSFC, Nos. 11604202, 11674213, 61735010 and 51372149). ZJ thanks the Young Eastern Scholar (QD2015020) at Shanghai Institutions of Higher Learning, and the Colleges. 'Chen Guang' project (16CG45) supported by Shanghai Municipal Education Commission and Shanghai Education Development Foundation. Universities Young Teachers Training Funding Program of Shanghai Municipal Education Commission (ZZSD15098).

ORCID iDs

Zuanming Jin https://orcid.org/0000-0002-9686-7965

References

[1] White R L 1969 Review of recent work on the magnetic and spectroscopic properties of the rare-earth orthoferrites *J. Appl. Phys.* **40** 1061–9
[2] Vahaplar K *et al* 2012 All-optical magnetization reversal by circularly polarized laser pulses: experiment and multiscale modeling *Phys. Rev.* B **85** 104402
[3] De Jong J A, Kimel A V, Pisarev R V, Kirilyuk A and Rasing T 2011 Laser-induced ultrafast spin dynamics in $ErFeO_3$ *Phys. Rev.* B **84** 104421
[4] De Jong J A, Razdolski I, Kalashnikova A M, Pisarev R V, Balbashov A M, Kirilyuk A, Rasing Th and Kimel A V 2012 Coherent control of the route of an ultrafast magnetic phase transition via low-amplitude spin precession *Phys. Rev. Lett.* **108** 157601
[5] Kimel A V, Stanciu C D, Usachev P A, Pisarev R V, Gridnev V N, Kirilyuk A and Rasing Th 2006 Optical excitation of antiferromagnetic resonance in $TmFeO_3$ *Phys. Rev.* B **74** 060403
[6] Kimel A V, Kirilyuk A, Tsvetkov A, Pisarev R V and Rasing T 2004 Laser-induced ultrafast spin reorientation in the antiferromagnet $TmFeO_3$ *Nature* **429** 850
[7] Jiang J, Jin Z, Song G, Lin X, Ma G and Cao S 2013 Dynamical spin reorientation transition in $NdFeO_3$ single crystal observed with polarized terahertz time domain spectroscopy *Appl. Phys. Lett.* **103** 062403
[8] Yamaguchi K, Kurihara T, Minami Y, Nakajima M and Suemoto T 2013 Terahertz time-domain observation of spin reorientation in orthoferrite $ErFeO_3$ through magnetic free induction decay *Phys. Rev. Lett.* **110** 137204
[9] Yamaguchi K, Nakajima M and Suemoto T 2010 Coherent control of spin precession motion with impulsive magnetic fields of half-cycle terahertz radiation *Phys. Rev. Lett.* **105** 237201
[10] Jin Z M, Mics Z, Ma G H, Cheng Z X, Bonn M and Turchinovich D 2013 Single-pulse terahertz coherent control of spin resonance in the canted antiferromagnet $YFeO_3$, mediated by dielectric anisotropy *Phys. Rev.* B **87** 094422
[11] Zhou R Z, Jin Z M, Li G F, Ma G H, Cheng Z X and Wang X L 2012 Terahertz magnetic field induced coherent spin precession in $YFeO_3$ *Appl. Phys. Lett.* **100** 061102
[12] Mikhaylovskiy R V, Hendry E, Kruglyak V V, Pisarev R V, Rasing Th and Kimel A V 2014 Terahertz emission spectroscopy of laser-induced spin dynamics in $TmFeO_3$ and $ErFeO_3$ orthoferrites *Phys. Rev.* B **90** 184405
[13] Lin X, Jiang J J, Jin Z M, Wang D Y, Tian Z, Han J G, Cheng Z X and Ma G H 2015 Terahertz probes of magnetic field induced spin reorientation in $YFeO_3$ single crystal *Appl. Phys. Lett.* **106** 092403
[14] Tokunaga Y, Furukawa N, Sakai H, Taguchi Y, Arima T-H and Tokura Y 2009 Composite domain walls in a multiferroic perovskite ferrite *Nat. Mater.* **8** 558
[15] Rajeswaran B, Sanyal D, Chakrabarti M, Sundarayya Y, Sundaresan A and Rao C N R 2013 Interplay of 4f–3d magnetism and ferroelectricity in $DyFeO_3$ *Europhys. Lett.* **101** 17001
[16] Tokura Y, Seki S and Nagaosa N 2014 Multiferroics of spin origin reports on *Prog. Phys.* **77** 076501
[17] Tokunaga Y, Iguchi S, Arima T and Tokura Y 2008 Magnetic-field-induced ferroelectric state in $DyFeO_3$ *Phys. Rev. Lett.* **101** 097205
[18] Mikhaylovskiy R V *et al* 2015 Ultrafast optical modification of exchange interactions in iron oxides *Nat. Commun.* **6** 8190
[19] Keffer F and Kittel C 1952 Theory of antiferromagnetic resonance *Phys. Rev.* **85** 329

[20] Geller S 1956 Crystal structure of gadolinium orthoferrite, $GdFeO_3$ *J. Chem. Phys.* **24** 1236–9
[21] Dzyaloshinskii I 1958 A thermodynamic theory of 'weak' ferromagnetism of antiferromagnetics *J. Phys. Chem. Solids* **4** 241–55
[22] Moriya T 1960 Anisotropic superexchange interaction and weak ferromagnetism *Phys. Rev.* **120** 91
[23] Zhao W Y, Cao S X, Huang R X, Cao Y M, Xu K, Kang B J, Zhang J C and Ren W 2015 Spin reorientation transition in dysprosium-samarium orthoferrite single crystals *Phys. Rev.* B **91** 104425
[24] Zhang K L, Xu K, Liu X M, Zhang Z Y, Jin Z M, Lin X, Li B, Cao S X and Ma G H 2016 Resolving the spin reorientation and crystal-field transitions in $TmFeO_3$ with terahertz transient *Sci. Rep.* **6** 23648
[25] Fu X J, Zeng X X, Wang D Y, Zhang H C, Han J G and Cui T J 2015 Ultralow temperature terahertz magnetic thermodynamics of perovskite-like $SmFeO_3$ ceramic *Sci. Rep.* **5** 14777
[26] Prelorendjo L A, Johnson C E, Thomas M F and Wanklyn B M 1980 Spin reorientation transitions in $DyFeO_3$ induced by magnetic fields *J. Phys.* C **13** 2567
[27] Baierl S, Hohenleutner M, Kampfrath T, Zvezdin A K, Kimel A V, Huber R and Mikhaylovskiy R V 2016 Nonlinear spin control by terahertz-driven anisotropy fields *Nat. Photon.* **10** 715
[28] Pedersen J E and Keiding S R 1992 THz time-domain spectroscopy of nonpolar liquids *IEEE J. Quantum Electron.* **28** 2518–22
[29] Nakajima M, Namai A, Ohkoshi S and Suemoto T 2010 Ultrafast time domain demonstration of bulk magnetization precession at zero magnetic field ferromagnetic resonance induced by terahertz magnetic field *Opt. Express* **18** 18260–8
[30] Jin Z M, Tkach A, Casper F, Spetter V, Grimm H, Thomas A, Kampfrath T, Bonn M, Kläui M and Turchinovich D 2015 Accessing the fundamentals of magnetotransport in metals with terahertz probes *Nat. Phys.* **11** 761
[31] Walowski J and Münzenberg M 2016 Perspective: Ultrafast magnetism and THz spintronics *J. Appl. Phys.* **120** 140901
[32] Huisman T J *et al* 2016 Femtosecond control of electric currents in metallic ferromagnetic heterostructures *Nat. Nano* **11** 455
[33] Nicoletti D and Cavalleri A 2016 Nonlinear light–matter interaction at terahertz frequencies *Adv. Opt. Photon.* **8** 401–64
[34] Kubacka T *et al* 2014 Large-amplitude spin dynamics driven by a THz pulse in resonance with an electromagnon *Science* **343** 1333
[35] Mukai Y, Hirori H, Yamamoto T, Kageyama H and Tanaka K 2014 Antiferromagnetic resonance excitation by terahertz magnetic field resonantly enhanced with split ring resonator *Appl. Phys. Lett.* **105** 022410
[36] Nishitani J, Kozuki K, Nagashima T and Hangyo M 2010 Terahertz radiation from coherent antiferromagnetic magnons excited by femtosecond laser pulses *Appl. Phys. Lett.* **96** 221906
[37] Fu X, Xi X, Bi K and Zhou J 2013 Temperature-dependent terahertz magnetic dipole radiation from antiferromagnetic $GdFeO_3$ ceramics *Appl. Phys. Lett.* **103** 211108
[38] Song G, Jiang J, Wang X, Jin Z, Lin X, Ma G and Cao S 2013 Selective excitation of spin resonance in orthoferrite $PrFeO_3$ with impulsive polarized terahertz radiation *J. Appl. Phys.* **114** 243104
[39] Jiang J, Song G, Wang D, Jin Z, Tian Z, Lin X, Han J, Ma G, Cao S and Cheng Z 2016 Magnetic-field dependence of strongly anisotropic spin reorientation transition in $NdFeO_3$: a terahertz study *J. Phys.: Condens. Mater* **28** 116002
[40] Suemoto T, Nakamura K, Kurihara T and Watanabe H 2015 Magnetization-free measurements of spin orientations in orthoferrites using terahertz time domain spectroscopy *Appl. Phys. Lett.* **107** 042404
[41] Bocklage L 2016 Model of THz magnetization dynamics *Sci. Rep.* **6** 22767
[42] Rietveld W J, Tordoir W E, Hagenouw J R, Lubbers J A and Spoor T A 1967 Visual evoked responses to blank and to checkerboard patterned flashes *Acta Physiol. Pharmacol. Neerl.* **14** 259–85
[43] Constable E, Cortie D L, Horvat J, Lewis R A, Cheng Z, Deng G, Cao S, Yuan S and Ma G 2014 Complementary terahertz absorption and inelastic neutron study of the dynamic anisotropy contribution to zone-center spin waves in a canted antiferromagnet $NdFeO_3$ *Phys. Rev.* B **90** 054413
[44] Yamaguchi K, Kurihara T, Watanabe H, Nakajima M and Suemoto T 2015 Dynamics of photoinduced change of magnetoanisotropy parameter in orthoferrites probed with terahertz excited coherent spin precession *Phys. Rev.* B **92** 064404
[45] Kampfrath T, Sell A, Klatt G, Pashkin A, Mährlein S, Dekorsy T, Wolf M, Fiebig M, Leitenstorfer A and Huber R 2011 Coherent terahertz control of antiferromagnetic spin waves *Nat. Photon.* **5** 31–4
[46] Bowlan P, Trugman S A, Bowlan J, Zhu J-X, Hur N J, Taylor A J, Yarotski D A and Prasankumar R P 2016 Probing ultrafast spin dynamics through a magnon resonance in the antiferromagnetic multiferroic $HoMnO_3$ *Phys. Rev.* B **94** 100404
[47] Watanabe H, Kurihara T, Kato T, Yamaguchi K and Suemoto T 2017 Observation of long-lived coherent spin precession in orthoferrite $ErFeO_3$ induced by terahertz magnetic fields *Appl. Phys. Lett.* **111** 092401
[48] Mukai Y, Hirori H, Yamamoto T, Kageyama H and Tanaka K 2016 Nonlinear magnetization dynamics of antiferromagnetic spin resonance induced by intense terahertz magnetic field *New J. Phys.* **18** 013045
[49] Lu J, Li X, Hwang H Y, Ofori-Okai B K, Kurihara T, Suemoto T and Nelson K A 2017 Coherent two-dimensional terahertz magnetic resonance spectroscopy of collective spin waves *Phys. Rev. Lett.* **118** 207204